

# First Observational Evidence for Split Infall Flow of Cosmic Filaments into Clusters

Ji Yao<sup>1,2\*</sup>, Huanyuan Shan<sup>1,2\*</sup>, Pengjie Zhang<sup>3,4,5</sup>,  
 Xiaohu Yang<sup>3,4,5</sup>, Jiale Zhou<sup>3</sup>, Jiaxin Han<sup>3,4,5</sup>, Peng Wang<sup>1,2</sup>

<sup>1</sup>Shanghai Astronomical Observatory (SHAO), Nandan Road 80,  
 Shanghai, 200030, China.

<sup>2</sup>University of Chinese Academy of Sciences, Beijing, 101408, China.

<sup>3</sup>Department of Astronomy, School of Physics and Astronomy, Shanghai  
 Jiao Tong University, Shanghai, 200240, China.

<sup>4</sup>Key Laboratory for Particle Astrophysics and Cosmology  
 (MOE)/Shanghai Key Laboratory for Particle Physics and Cosmology,  
 Shanghai, 200240, China.

<sup>5</sup>Tsung-Dao Lee Institute, Shanghai Jiao Tong University, Shanghai,  
 200240, China.

\*Corresponding author(s). E-mail(s): [ji.yao@shao.ac.cn](mailto:ji.yao@shao.ac.cn);  
[hyshan@shao.ac.cn](mailto:hyshan@shao.ac.cn);

## Abstract

Velocity fields in the cosmic web are fundamental to structure formation but remain difficult to observe directly beyond the linear regime. Here we present observational evidence that galaxy filaments connecting pairs of galaxy clusters undergo a split infall, with opposite velocity flows toward the two clusters. Using spectroscopic galaxies from the Sloan Digital Sky Survey, we isolate the internal filament velocity field by subtracting its rigid-body background motion and Hubble flow, and detect this effect at greater than  $5\sigma$  significance across a wide range of cluster and filament selections. The measured velocity profile exhibits a sign reversal near the filament midpoint and a maximum infall amplitude of  $\sim 30$  km/s ( $\sim 20$  km/s projected onto the line-of-sight) for clusters of mass  $\sim 10^{14.3} M_\odot$ , substantially lower than expected for infall from an average cosmic environment. Multiple results on density-velocity correlation, mass-dependency, and validation with simulation indicate that filaments dynamically respond to competing gravitational potentials rather than acting as passive mass transport channels. Our results establish a new observational window on quasi-linear

velocity fields in the cosmic web and provide a promising probe of mass measurement, testing gravity and velocity reconstruction with upcoming wide-field spectroscopic surveys.

**Keywords:** cluster, filament, velocity, large-scale structure

## 1 Introduction

The velocity field is a fundamental probe of cosmic structure formation, encoding the growth of density perturbations and the action of gravity across both linear and non-linear regimes [1, 2]. It governs matter transport within the cosmic web [3], the assembly of dark matter haloes and galaxy clusters [4–8], and the dynamics of filaments connecting these dense nodes [9, 10], as well as galaxy and gas motions on smaller scales [11, 12]. Despite its central role, direct observational access to velocity fields beyond the linear regime remains limited. In galaxy surveys, redshifts combine contributions from cosmic expansion and peculiar motions, making it difficult to isolate velocities without additional modelling [13]. Velocity reconstruction techniques infer velocity fields from density maps under assumptions of gravitational instability [14, 15], while the kinetic Sunyaev-Zeldovich effect probes electron motions through secondary cosmic microwave background anisotropies [16–19]. However, both approaches face practical and conceptual limitations, particularly on quasi-linear and non-linear scales [20, 21].

Regarding structure-specific velocity fields, extensive research has characterized the infall patterns and angular momentum of clusters and filaments [9, 10, 22], as well as their complex correlations with underlying density fields and host halo properties [4–6, 23–29]. However, the velocity interaction between clusters and filaments, which is a critical part of cosmic structure formation, remains largely unexplored through direct observation [30].

In this work, we investigate the internal velocity field of filaments in cluster-filament-cluster systems identified in the Sloan Digital Sky Survey (SDSS) galaxy group catalogues [31–33], and test whether filamentary flows exhibit a split infall pattern under the competing gravitational influence of clusters on both sides. By exploiting the geometry of cluster pairs, we can resolve velocity flows along different segments of the filament and directly measure velocity gradients on quasi-linear scales. This provides complementary information to density-based velocity reconstruction, which primarily probes the linear regime. It also provides direct insight into how matter is supplied to galaxy clusters through the cosmic web [34].

## 2 Results

Observationally, it is difficult to directly see how a filament falls into galaxy clusters, while this effect is expected in both gravitational theory and cosmological simulations. The key problem is the degeneracy between Hubble flow and peculiar velocity: in galaxy surveys, the observed redshift of a single galaxy contains cosmological redshift

due to Hubble flow <sup>1</sup> and Doppler redshift due to peculiar velocity. This problem can be reconsidered when a filament exists between a pair of clusters, as in this work we propose a simple design to find how the filament falls separately into the two clusters, which includes: how fast the infall flow is, the behavior of this flow, and how the flow responds to mass.

The components that build up the redshift distribution of a filament are resolved as: Hubble flow, rigid-body motions including translation and rotation, a dynamical flow motion on top of the rigid-body, and pairwise velocity of the two clusters as a background that linearly stretches or compresses the filament. We find that redshift introduced by each term, except the dynamical flow of the filament itself, scales as  $z \propto v \propto r$ , where  $v$  here denotes different types of velocity, and  $r$  denotes the distance to the close cluster projected on the filament direction. Therefore, one can linearly interpolate a “rigid-body background” redshift at each point on the filament based on the two clusters at two ends, and subtracting this background redshift effectively subtract the Hubble flow, while fixing the velocity of the two clusters at zero. Consequently, the excess redshift  $\Delta z$  after subtracting the rigid-body background motion will come from the flow motion on the filament.

We find a non-vanishing flow on the filament direction by stacking 360 filaments defined from SDSS group catalog (see Sec. 5 for details), with the flow-induced excess redshift of each galaxy visualized in Fig. 1. Relative to the rigid-body background shown as a x-axis, we observe a flow motion with a slope  $(1.21 \pm 0.22) \times 10^{-4}$ , i.e.  $5.5\sigma$  significance. To better understand how this velocity flow falls into the clusters, we divide the normalized filament length into 10 bins and calculate the mean velocity in each bin. The resulting mean velocity profile is shown in Fig. 2. This signal rejects the null hypothesis at  $5.6\sigma$ , which is consistent with the significance of the slope fitting in Fig. 1. At the close end, the negative excess redshift ( $\Delta z < 0$ ) indicates that material within the filament is moving towards us (the observer), while at the far end, it is receding from us ( $\Delta z > 0$ ).

Symmetry considerations allow for a deeper understanding of this flow motion. The motion beyond rigid-body background could arise from three effects: (1) inflow toward the two clusters; (2) rotational flow around an axis offset from the filament; (3) spinning flow around the long axis of the filament. Due to the isotropy required by the cosmological principle (there is no preferred direction in the Universe), when stacking many filament systems, the contributions from filaments with rotation-in and rotation-out flows should cancel out. Therefore, the filament rotational flow described in (2) should not contribute to the signal in Fig. 1 and 2. Similarly, the contributions from spin-in and spin-out flows should cancel, so the filament spinning flow described in (3) should also not contribute. Consequently, the observed flow represents the inflow toward the two clusters. By projecting this flow velocity onto the line-of-sight direction (i.e., the z-direction), we obtain the flow-induced excess redshift  $\Delta z$  according to:  $v_z = v \times \cos\langle \hat{f}, \hat{z} \rangle = c\Delta z$ , where  $v$  is the flow velocity along the filament,  $\hat{f}$  is the filament direction pointing from the close cluster to the distant cluster,  $\hat{z}$  is the line-of-sight direction,  $c$  is the speed of light.

---

<sup>1</sup> $v = H_0 r$ , two space separated by distance  $r$  are effectively leaving apart at velocity  $v$  controled by the Hubble constant  $H_0$

We find several physical features of this filament flow:

(a) The amplitude of the infall velocity has a trend of increase-maximum-decrease from the cluster center towards outside along the filament, which agrees with the depletion radius feature of general dark matter halos in N-body simulation [4]. The maximum infall velocity toward each cluster with mass  $m \sim 10^{14.3} M_{\odot}$  at redshift  $z \sim 0.059$  reaches  $v_{\max} \sim 30$  km/s, whose projection on the line-of-sight is  $v_{z,\max} \sim 20$  km/s <sup>2</sup>.

(b) The depletion radius, where the infall velocity into the cluster is maximized, is sensitive to the mass distribution in the system. In the observation (Fig. 2), this position is at  $\sim 0.15$  of the filament length (2-6 Mpc, 4.7 Mpc on average), so overall  $< 1$  Mpc from the cluster center. For comparison, in N-body simulation, for a single halo with such mass but average environment density, this position is at  $\sim 3$  Mpc from the halo center with maximum infall velocity  $> 400$  km/s after removing Hubble flow (Fig. C6). For a simulated halo-halo system in an average cosmological environment (without an intervening filament), this position is at  $\sim 1.4$  Mpc from the halo center with maximum infall velocity  $\sim 60$  km/s (Fig. C8). This is due to the presence of the filament and the other cluster as a special environment, and we refer to Appendix C for a more detailed demonstration.

(c) The galaxy line-density is anti-correlated to the amplitude of this flow in the filament. In Fig. 1, the velocity flow is zero at the filament's midpoint and peaks near the two ends, meanwhile, in the galaxy number count distribution, it suggests the density of the filament peaks at the center and decreases at two ends. We demonstrate this density is not due to the redshift-space distortion (RSD) and the cylindrical selection function in Fig. C9, but due to filament dynamics. This behavior is consistent with the continuity equation, which in a cylindrical filament approximation writes:  $d(A \times v \times \rho)/dt = 0$ , where  $A$  denotes the area,  $v$  denotes the velocity of the flow, and  $\rho$  denotes the density. The density-velocity co-evolution additionally supports depletion radius as a clear boundary between the cluster and the filament. This point will be further confirmed in the cluster-mass-dependency result next.

Besides the symmetry argument discussed previously, further evidence that this flow is driven by the gravity of the cluster pair comes from its mass-dependency. In Fig. 3, we see that when the close cluster is at least twice as massive, the excess redshift  $\Delta z$  on the filament becomes more negative, indicating that a larger portion of the filament is flowing toward the more massive cluster, and vice versa when the distant cluster is more massive. Under such mass imbalance, both the projected peak infall velocity ( $\sim 60$  km/s) and location of depletion radius ( $\sim 0.2$  of the filament length) increase compared to those in Fig. 2 ( $\sim 20$  km/s at  $\sim 0.15$ ), demonstrating the growing gravitational dominance of the more massive cluster in the system.

---

<sup>2</sup> Assuming the line connecting cluster A and cluster B is isotropically oriented, a shell integral gives  $\bar{v}_z = \langle v \cos \theta \rangle = \frac{\int_0^{\pi/2} \int_0^{\pi/2} v \cos \theta \sin \theta d\theta d\phi}{\int_0^{\pi/2} \int_0^{\pi/2} \sin \theta d\theta d\phi} = \frac{1}{2} \bar{v}$ . We confirm the mean projection effect of  $\langle \cos \theta \rangle \sim 0.5$  in Fig. A1. But we note this is the mean value, while the actual value can vary at different location. A deprojected velocity profile can be found in Fig. C8.

### 3 Summary and Discussion

Physically, both theory and simulations predict mass flow from less massive regions into more massive ones. In this work, we present a straightforward design to remove Hubble flow with the first measurement of how a filament get split and fall separately into the clusters at two ends (Fig. 2). We validate this flow is gravity-driven via three independent perspectives:

- (1) Observationally, we show the amplitude of the flow is anti-correlated to galaxy-line-density (Fig. 1), which is expected from the continuity equation.
- (2) Also in observation, we show the velocity profile of the flow is sensitive to the mass of the clusters at two sides (Fig. 3).
- (3) Theoretically, the measured velocity profile agrees with our model constructed from N-body simulation (Appendix C).

We therefore establish that this flow is gravity-induced, with a significance exceeding  $5\sigma$ . Some details of this flow and their interpretations are discussed as follows.

This flow delineates a clear boundary between the filament and the cluster, where the infall velocity is maximized (Fig. 2) and galaxy line-number-density is minimized (Fig. 1). This feature is similar to the depletion radius of dark matter halos [4] governed by the continuity equation, while the difference is that the filament here plays the role of a special environment while the clusters at two ends slowly “steal” matter from it. In addition, we demonstrate that the change in galaxy line-number-density should come from the filament dynamics by comparing with the selection effect from cylindrical filament and RSD introduced density-redistribution (Fig. C9 and Appendix C).

On the other hand, this infall velocity profile and the corresponding “depletion radius” in our cluster are very sensitive to the mass distribution in the system, including both the clusters and the filament. In observation, when increasing the mass at one end while reducing the mass at the other end, the projected infall flow at the more massive end will significantly increase (from  $\sim 20$  to  $\sim 60$  km/s), together with the depletion radius increases as this cluster becomes more dominant in the system (Fig. 3.). Nonetheless, in our model constructed from N-body simulation (Appendix C ), we show step-by-step how the infall flow changes from single halo case (Fig. C6) to halo-halo without a connecting filament, and then to halo-filament-halo scenarios (Fig. C8). We show the observed velocity profile is consistent with the halo-filament-halo case, and is smaller than the halo-halo without filament case, being an order of magnitude smaller than the single halo case. This difference is attributed to the balance from the filament and the cluster at the other end, which significantly weakens the tidal gravitational field. The fact that a more massive environment can make depletion radius shrink is also seen in N-body simulation [4]. We additionally note that the balanced gravity from the environment is not the only reason the amplitude of our observed flow is smaller than the single halo case, as the excess redshift  $\Delta z$  also removes the pairwise velocity of the two clusters.

Despite the observed flow agreeing with our model well, we note there exists a 0.4 dex mismatch in the filament mass. The optically derived mean mass for the filament is  $M_{200c} \sim 10^{13.32} M_\odot$  in Fig. A1, while in our model we need to put a  $M_{200c} \sim 10^{13.71} M_\odot$  halo at the filament center to reproduce the observed flow, shown in Fig. C8. This 0.4 dex difference could be due to the limits of our model, which uses a concentrated

spherical halo in a WMAP  $\Lambda$ CDM cosmology to represent the flat filament. It could also come from the richness cut  $\lambda_f < 5$  for the filament that potentially biases the mass estimation [35]. Still, the 0.4 dex is acceptable in terms of mass measurement. Meanwhile, the fact that the system is sensitive to the filament mass makes it a powerful tool in future mass-constraints for dark matter.

The observed excess redshift  $\Delta z$  (Fig. 2) can be interpreted not only as velocity flow, but also as redshift-space distortion (RSD) [36, 37], which suggests that the galaxy distribution around the two clusters is compressed in the z-direction due to the Kaiser effect. The Kaiser effect can be further visualized in Fig. C9, where the distorted space actually corresponds to the velocity flows in Fig. 2 and C8. Nonetheless, the  $\Delta z$  in Fig. 1 is widely distributed along the z-direction around the linear-fit, which contains not only redshift measurement error, but also the Finger-of-God (FoG) effect, reflecting contributions from galaxies that build not only the clusters but also the filament.

There are two extra phenomena we expect but do not observe due to insufficient S/N (signal-to-noise ratio) with limited number of spectroscopic galaxies. One is the break at the center of the filament when the infall flow has existed for a sufficient duration: in Fig. 1 and C9 we see the galaxy-line-density of the filament deviates from the single-peak distribution, however the significance is low. But we do expect this phenomenon as the velocity in Fig. C8 and C7 suggest the out-going flow overcomes the in-going flow of the filament right outside the filament center. The other is the possible tidal disruption of the less massive cluster if we keep increasing the mass-ratio in Fig. 3, which could provide deeper insight into halo/cluster merger dynamics and offer valuable information on observational merger histories.

Previous studies have looked into cluster growth, cluster spins, filament spins independently [6, 10, 24, 38], while correlations between cluster spin and filaments-cluster alignment have also been found [30]. Our finding of how a filament falls into a cluster therefore serves as an important bridge connecting these previously disparate results. It also provides an independent view of how matter and angular momentum are transferred in such a complex non-linear environment.

In the near future, when more powerful spectroscopic data (DESI [39], PFS [40], MUST [41], JUST [42], EAST <sup>3</sup>, etc.) become available, one can further observe this filament flow and investigate its dependency on redshift, cluster mass and filament mass as a complete setup, which should provide strong S/N and opens a new window for examining gravity and constraining dark matter particle mass, as this flow is clearly sensitive to mass in the non-linear regime (Fig. C8). Meanwhile, this flow can help in segmenting the observational data to trace the physical process of galaxies traveling through the filament-boundary-cluster timeline, and investigate properties like galaxy shape alignments and galaxy colors [43, 44]. By combining with SZ or X-ray observations one can further understand the dynamical co-evolution of gas and structure formation.

---

<sup>3</sup>[https://astro.pku.edu.cn/research/PKU\\_EAST\\_ENG.htm](https://astro.pku.edu.cn/research/PKU_EAST_ENG.htm)

## References

- [1] Zhang, P., Liguori, M., Bean, R. & Dodelson, S. Probing gravity at cosmological scales by measurements which test the relationship between gravitational lensing and matter overdensity. *Phys. Rev. Lett.* **99**, 141302 (2007). URL <https://link.aps.org/doi/10.1103/PhysRevLett.99.141302>.
- [2] Hahn, O., Angulo, R. E. & Abel, T. The properties of cosmic velocity fields. *Monthly Notices of the Royal Astronomical Society* **454**, 3920–3937 (2015).
- [3] Cautun, M., van de Weygaert, R., Jones, B. J. T. & Frenk, C. S. Evolution of the cosmic web. *Monthly Notices of the Royal Astronomical Society* **441**, 2923–2973 (2014).
- [4] Fong, M. & Han, J. A natural boundary of dark matter haloes revealed around the minimum bias and maximum infall locations. *mnras* **503**, 4250–4263 (2021).
- [5] Zhou, Y. & Han, J. A physical and concise halo model based on the depletion radius. *Monthly Notices of the Royal Astronomical Society* **525**, 2489–2508 (2023).
- [6] Zhou, Y. & Han, J. Einasto Profile as the Halo Model Solution Coupled to the Depletion Radius. *The Astrophysical Journal* **979**, 55 (2025).
- [7] Sheth, R. K., Hui, L., Diaferio, A. & Scoccimarro, R. Linear and non-linear contributions to pairwise peculiar velocities. *Monthly Notices of the Royal Astronomical Society* **325**, 1288–1302 (2001).
- [8] Jing, Y. P., Mo, H. J. & Börner, G. Spatial Correlation Function and Pairwise Velocity Dispersion of Galaxies: Cold Dark Matter Models versus the Las Campanas Survey. *The Astrophysical Journal* **494**, 1–12 (1998).
- [9] Libeskind, N. I., Tempel, E., Hoffman, Y., Tully, R. B. & Courtois, H. Filaments from the galaxy distribution and from the velocity field in the local universe. *Monthly Notices of the Royal Astronomical Society* **453**, L108–L112 (2015).
- [10] Wang, P., Libeskind, N. I., Tempel, E., Kang, X. & Guo, Q. Possible observational evidence for cosmic filament spin. *Nature Astronomy* **5**, 839–845 (2021).
- [11] Li, Z.-Z. & Han, J. The Outermost Edges of the Milky Way Halo from Galaxy Kinematics. *The Astrophysical Journal Letters* **915**, L18 (2021).
- [12] Faucher-Giguère, C.-A. & Oh, S. P. Key Physical Processes in the Circumgalactic Medium. *Annual Review of Astronomy and Astrophysics* **61**, 131–195 (2023).
- [13] Abdalla, E. *et al.* Cosmology intertwined: A review of the particle physics, astrophysics, and cosmology associated with the cosmological tensions and anomalies. *Journal of High Energy Astrophysics* **34**, 49–211 (2022).

- [14] Yu, Y., Zhu, H.-M. & Pen, U.-L. Halo Nonlinear Reconstruction. *The Astrophysical Journal* **847**, 110 (2017).
- [15] Xiao, X. *et al.* AI-powered Reconstruction of Dark Matter Velocity Fields from Redshift-space Halo Distribution. *The Astrophysical Journal* **994**, 204 (2025).
- [16] Chen, Z., Zhang, P., Yang, X. & Zheng, Y. Detection of pairwise kSZ effect with DESI galaxy clusters and Planck. *Monthly Notices of the Royal Astronomical Society* **510**, 5916–5928 (2022).
- [17] Chen, Z., Zhang, P. & Yang, X. Thermal Energy Census with the Sunyaev-Zel'dovich Effect of DESI Galaxy Clusters/Groups and Its Implication on the Weak-lensing Power Spectrum. *The Astrophysical Journal* **953**, 188 (2023).
- [18] Zheng, Y., Zhang, P., Jing, Y., Lin, W. & Pan, J. Peculiar velocity decomposition, redshift space distortion, and velocity reconstruction in redshift surveys. II. Dark matter velocity statistics. *Physical Review D* **88**, 103510 (2013).
- [19] Li, S., Zheng, Y., Chen, Z., Xu, H. & Yang, X. Detection of Pairwise Kinetic Sunyaev-Zel'dovich Effect with DESI Galaxy Groups and Planck in Fourier Space. *Astrophysical Journal Supplement Series* **271**, 30 (2024).
- [20] Stiskalek, R. *et al.* The Velocity Field Olympics: Assessing velocity field reconstructions with direct distance tracers. *Monthly Notices of the Royal Astronomical Society* (2025).
- [21] Aghanim, N., Górski, K. M. & Puget, J.-L. How accurately can the SZ effect measure peculiar cluster velocities and bulk flows? *Astronomy and Astrophysics* **374**, 1–12 (2001).
- [22] Diaferio, A. & Geller, M. J. Infall Regions of Galaxy Clusters. *Astrophysical Journal* **481**, 633–643 (1997).
- [23] More, S., Diemer, B. & Kravtsov, A. V. The Splashback Radius as a Physical Halo Boundary and the Growth of Halo Mass. *Astrophysical Journal* **810**, 36 (2015).
- [24] Gabriel-Silva, L. & Sodré, L., Jr. Galaxy Cluster Mass Estimation through the Splashback Radius. *The Astrophysical Journal* **988**, 149 (2025).
- [25] Hahn, O., Carollo, C. M., Porciani, C. & Dekel, A. The evolution of dark matter halo properties in clusters, filaments, sheets and voids. *Monthly Notices of the Royal Astronomical Society* **381**, 41–51 (2007).
- [26] Codis, S., Pichon, C. & Pogosyan, D. Spin alignments within the cosmic web: a theory of constrained tidal torques near filaments. *Monthly Notices of the Royal Astronomical Society* **452**, 3369–3393 (2015).

- [27] Yang, X. *et al.* An Extended Halo-based Group/Cluster Finder: Application to the DESI Legacy Imaging Surveys DR8. *The Astrophysical Journal* **909**, 143 (2021).
- [28] Yang, X. *et al.* The cross-correlation between galaxies and groups: probing the galaxy distribution in and around dark matter haloes. *Monthly Notices of the Royal Astronomical Society* **362**, 711–726 (2005).
- [29] Yang, X., Mo, H. J., van den Bosch, F. C. & Jing, Y. P. A halo-based galaxy group finder: calibration and application to the 2dFGRS. *Monthly Notices of the Royal Astronomical Society* **356**, 1293–1307 (2005).
- [30] Tang, X.-x., Wang, P., Rong, Y., cui, W. & Bao, M. The Cosmic Dance: Observational Detection of Coherent Spin in Galaxy Clusters. *The Astrophysical Journal Letters* **995**, L9 (2025).
- [31] Tempel, E., Tuvikene, T., Kipper, R. & Libeskind, N. I. Merging groups and clusters of galaxies from the SDSS data. The catalogue of groups and potentially merging systems. *Astronomy and Astrophysics* **602**, A100 (2017).
- [32] Eisenstein, D. J. *et al.* SDSS-III: Massive Spectroscopic Surveys of the Distant Universe, the Milky Way, and Extra-Solar Planetary Systems. *The Astronomical Journal* **142**, 72 (2011).
- [33] Alam, S. *et al.* The Eleventh and Twelfth Data Releases of the Sloan Digital Sky Survey: Final Data from SDSS-III. *The Astrophysical Journal Supplement Series* **219**, 12 (2015).
- [34] Han, J., Cole, S., Frenk, C. S., Benitez-Llambay, A. & Helly, J. HBT+: an improved code for finding subhaloes and building merger trees in cosmological simulations. *Monthly Notices of the Royal Astronomical Society* **474**, 604–617 (2018).
- [35] Sun, Z. *et al.* Cross-correlation of Planck cosmic microwave background lensing with DESI galaxy groups. *Monthly Notices of the Royal Astronomical Society* **511**, 3548–3560 (2022).
- [36] Hamilton, A. J. S. Hamilton, D. (ed.) *Linear Redshift Distortions: a Review*. (ed. Hamilton, D.) *The Evolving Universe*, Vol. 231 of *Astrophysics and Space Science Library*, 185 (1998). [arXiv:astro-ph/9708102](https://arxiv.org/abs/astro-ph/9708102).
- [37] Percival, W. J. & White, M. Testing cosmological structure formation using redshift-space distortions. *Monthly Notices of the Royal Astronomical Society* **393**, 297–308 (2009).
- [38] Goldstein, S. & Hill, J. C. Evidence of galaxy cluster rotation in the cosmic microwave background. *arXiv e-prints* arXiv:2512.10951 (2025).

- [39] Abdul Karim, M. *et al.* DESI DR2 results. II. Measurements of baryon acoustic oscillations and cosmological constraints. *Physical Review D* **112**, 083515 (2025).
- [40] Takada, M. *et al.* Extragalactic science, cosmology, and Galactic archaeology with the Subaru Prime Focus Spectrograph. *Publications of the Astronomical Society of Japan* **66**, R1 (2014).
- [41] Zhao, C. *et al.* MULTiplexed Survey Telescope: Perspectives for Large-Scale Structure Cosmology in the Era of Stage-V Spectroscopic Survey. *arXiv e-prints* arXiv:2411.07970 (2024).
- [42] JUST Team *et al.* The Jiao Tong University Spectroscopic Telescope (JUST) Project. *Astronomical Techniques and Instruments* **1**, 16–30 (2024).
- [43] Yao, J. *et al.* KiDS-1000: Cross-correlation with Planck cosmic microwave background lensing and intrinsic alignment removal with self-calibration. *Astronomy and Astrophysics* **673**, A111 (2023).
- [44] Yao, J., Shan, H., Zhang, P., Kneib, J.-P. & Jullo, E. Unveiling the Intrinsic Alignment of Galaxies with Self-calibration and DECaLS DR3 Data. *The Astrophysical Journal* **904**, 135 (2020).
- [45] Wang, Y. *et al.* The clustering of the SDSS-IV extended baryon oscillation spectroscopic survey DR16 luminous red galaxy and emission-line galaxy samples: cosmic distance and structure growth measurements using multiple tracers in configuration space. *Monthly Notices of the Royal Astronomical Society* **498**, 3470–3483 (2020).
- [46] Hartlap, J., Simon, P. & Schneider, P. Why your model parameter confidences might be too optimistic. unbiased estimation of the inverse covariance matrix. *Astronomy and Astrophysics* **464**, 399–404 (2007). URL <https://doi.org/10.1051/0004-6361:20066170>.
- [47] Murata, R. *et al.* Constraints on the Mass-Richness Relation from the Abundance and Weak Lensing of SDSS Clusters. *The Astrophysical Journal* **854**, 120 (2018).
- [48] Chen, Z., Yu, Y., Han, J. & Jing, Y. CSST cosmological emulator I: Matter power spectrum emulation with one percent accuracy to  $k = 10h \text{ Mpc}^{-1}$ . *Science China Physics, Mechanics, and Astronomy* **68**, 289512 (2025).
- [49] Diemer, B. & Kravtsov, A. V. A Universal Model for Halo Concentrations. *The Astrophysical Journal* **799**, 108 (2015).
- [50] Jing, Y. CosmicGrowth Simulations—Cosmological simulations for structure growth studies. *Science China Physics, Mechanics, and Astronomy* **62**, 19511 (2019).

- [51] Jing, Y. P. & Suto, Y. Triaxial Modeling of Halo Density Profiles with High-Resolution N-Body Simulations. *The Astrophysical Journal* **574**, 538–553 (2002).
- [52] Han, J., Jing, Y. P., Wang, H. & Wang, W. Resolving subhaloes' lives with the Hierarchical Bound-Tracing algorithm. *Monthly Notices of the Royal Astronomical Society* **427**, 2437–2449 (2012).
- [53] Chisari, N. E. *et al.* Core Cosmology Library: Precision Cosmological Predictions for LSST. *The Astrophysical Journal Supplement Series* **242**, 2 (2019).
- [54] Duffy, A. R., Schaye, J., Kay, S. T. & Dalla Vecchia, C. Dark matter halo concentrations in the Wilkinson Microwave Anisotropy Probe year 5 cosmology. *Monthly Notices of the Royal Astronomical Society* **390**, L64–L68 (2008).

**Acknowledgements.** This work is supported by National Key R&D Program of China No. 2022YFF0503403. JY acknowledges the support from NSFC Grant No.12203084 and 12573006, the China Postdoctoral Science Foundation Grant No. 2021T140451, and the Shanghai Post-doctoral Excellence Program Grant No. 2021419. HYS acknowledges the support from NSFC of China under grant 11973070, the Shanghai Committee of Science and Technology grant No.19ZR1466600 and Key Research Program of Frontier Sciences, CAS, Grant No. ZDBS-LY-7013. PZ acknowledges the support of NSFC No. 11621303, the National Key R&D Program of China 2020YFC22016. ZF acknowledges the support from NSFC No. 11933002 and U1931210. This work is supported by the China Manned Space Program with grant no. CMS-CSST-2025-A03.

## 4 Figures

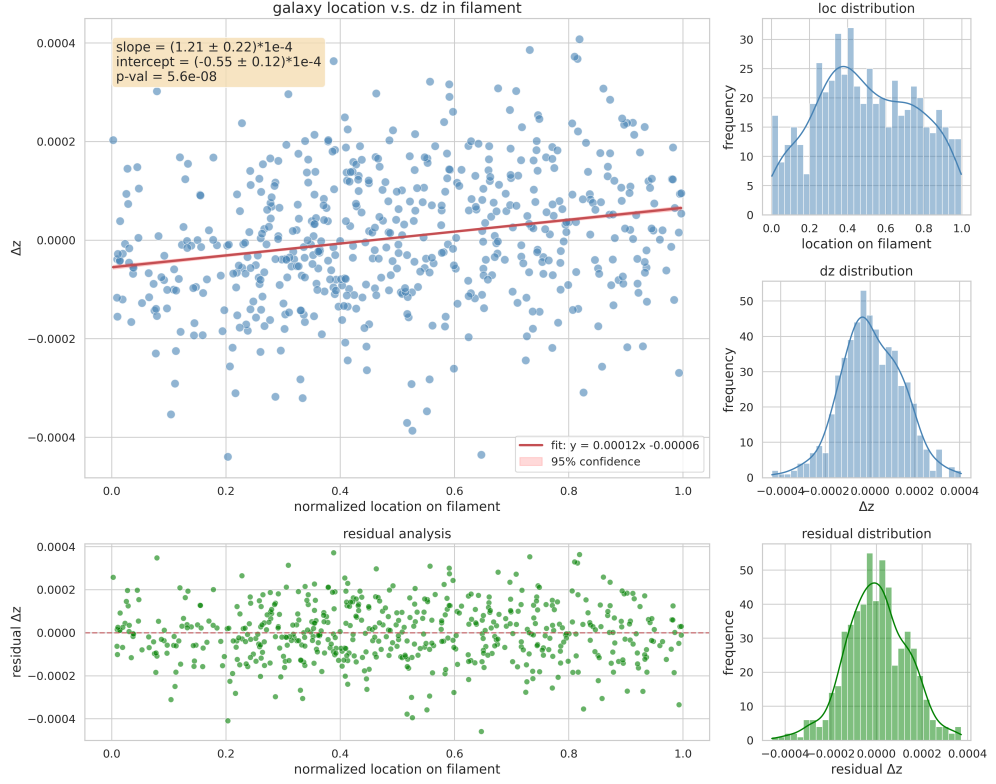


**Fig. 1** Distribution of the excess redshift of galaxies  $\Delta z$  after linearly subtracting rigid-body background redshift of the filament, representing the flow motion on the filament. The top-left panel shows the excess redshift  $\Delta z$  v.s. location on the filament, with each (blue) point representing a galaxy. We fit a line (red) to the points and get a slope that deviates from 0 at  $5.5\sigma$  significance, providing strong evidence that the filament is flowing from the center to the two sides. The top-right two panels show how the galaxies distribute on different locations and  $\Delta z$ . The non-uniform galaxy-line-density is not only due to selection effect, but also due to filament dynamics, see Fig. C9. The two bottom panels in green show the residual distribution after subtracting the linear fit.

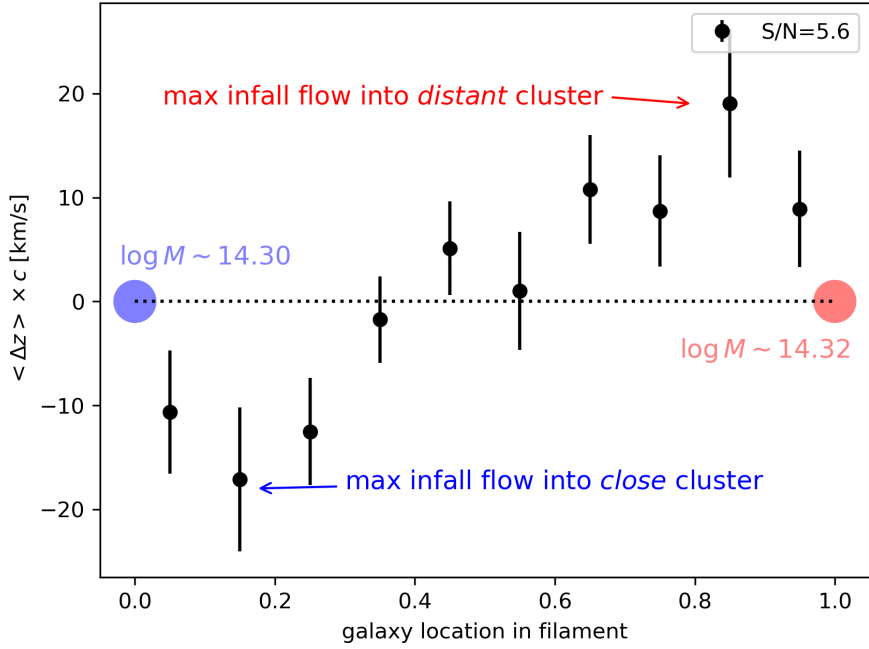


**Fig. 2** Mean velocity flow measurement along the filament. This figure uses the same data as Fig. 1, but divides into 10 bins to illustrate the spatial variation of the flow. The blue circle corresponds to the closer cluster (with mass  $\sim 10^{14.3} M_{\odot}$ ) and the red circle represents the more distant cluster (with mass  $\sim 10^{14.32} M_{\odot}$ ). The dotted line represents no velocity flow with respect to the “rigid-body” frame of the filament. The (black) data reject the null hypothesis at  $5.6\sigma$  significance, suggesting the filament is flowing from the center toward the two ends, reaching a maximum velocity at  $\sim 20$  km/s. The deprojected velocity profile along the filament direction and its comparisons with N-body simulation are shown in Fig. C8.

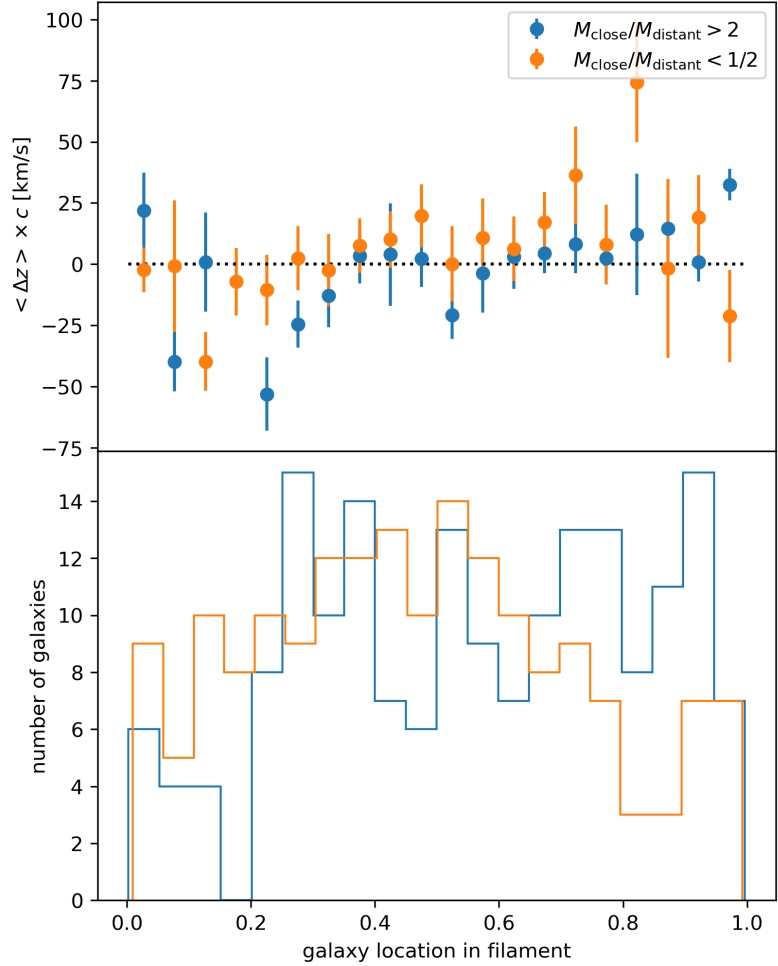


**Fig. 3** How unbalanced mass affects velocity flow (top) and galaxy distribution (bottom) on the filament. When we further divide the sample into unbalanced mass samples, whether the more massive cluster is at the near end (blue) or at the far end (orange), the filament is generally flowing towards it. Meanwhile, a larger peak velocity ( $\sim 50$  to  $75$  km/s) appears at a larger distance ( $\sim 0.2$ ) to the cluster center compared to Fig. 2. Significant dips can be found at the maximum infall place in the galaxy distribution.

## 5 Methods

In this work, we use SDSS spectroscopic galaxies and galaxy groups [31] to select clusters, filaments, and measure the flow motion. The methodology to extract the flow motion is straightforward:

- (1) In comoving space, we select a cluster pair (cluster A and B) that are sufficiently close ( $2 < L < 6$  Mpc, but not too close so that merging clusters and possible cross-contaminations are removed), and search for galaxies residing in a cylindrical space (width  $W < 1.2 \times r_{200c}$  where  $r_{200c}$  is the radius of the larger cluster) with the two clusters centered at its ends. These galaxies will represent the connecting filament between the cluster pair.
- (2) Define the filament axis as the straight line connecting the two clusters, and project each galaxy P with observed redshift  $z_i$  (for the i-th galaxy) onto the straight line to find their normalized location  $x_i = \vec{AP} \cdot \vec{AB} / \vec{AB}^2$  ( $0 < x_i < 1$ ) on the filament, with the close cluster A at location  $x_A = 0$  and the distant cluster B at location  $x_B = 1$ .
- (3) Linearly interpolate the redshift at each point on the line ( $z(x) = kx + b$ ) based on the two clusters (cluster A with  $x_A, z_A$  and cluster B with  $x_B, z_B$ ) at two ends. This will represent the redshift introduced by position (i.e. Hubble flow) and velocity along the line-of-sight direction, including translation and rotation as a cluster-cluster pair.
- (4) By subtracting the interpolated redshift in step (3) from the redshift of galaxies in step (2), one obtains the excess redshift  $\Delta z_i = z_i - z(x_i)$ , representing the *flow* motion beyond the rigid-body background motion in the filament frame. We note in this way the two clusters will have  $\Delta z = 0$ , so that their pairwise velocity is also removed.
- (5) Finally, considering a single filament does not contain enough galaxies to clearly describe the velocity flow, we choose to stack multiple filaments that satisfy the following criteria: cluster richness  $\lambda_c > 5$ , mass  $M_{200c} > 10^{13.5} M_\odot$ , filament richness  $1 < \lambda_f < 5$ , length  $2 < L < 6$  Mpc, width  $W < 1.2 \times r_{200c}$ .

After the above selections, we obtain 4728 galaxy groups as clusters, and only 360 systems of cluster-filament-cluster after the selection of filament length, width, and richness. We stack the filaments by putting the close cluster at  $x = 0$  and the distant cluster at  $x = 1$ . After linearly removing the rigid-body background motion and cluster pairwise velocity, we successfully obtain the excess redshift  $\Delta z_i$  data v.s. normalized location  $x_i$  in Fig. 1. Under the fiducial selection, the stacked filaments have the following average properties: length  $L = 4.7$  Mpc, width  $W = 1.6$  Mpc, cluster mass  $M_{200c} \sim 10^{14.3} M_\odot$ , filament mass  $M_f \sim 10^{13.32} M_\odot$ , and filament-redshift ( $\hat{f}, \hat{z}$ ) alignment angle  $\cos\langle\hat{f}, \hat{z}\rangle \sim 0.52$ , shown in Appendix A. We note that the radius definition  $r_{200c}$  and mass definition  $M_{200c}$  we use come from the group catalog [31] and are based on the halo profile density at 200 times the critical density of the Universe.

Fig. 2 is the binned average data of Fig. 1, where we divide the filament linearly into 10 bins. The statistical error and covariance in Fig. 2 are calculated with jackknife resampling, treating each cluster-filament-cluster system as an independent subsample. We find that the resulting covariance matrix is strongly diagonal, suggesting the leakage of galaxy from one bin to another is small, which at some level infers the velocity-location contamination from a single redshift (similar to redshift-space distortion, RSD) is not very significant. The S/N (signal-to-noise ratio) is calculated by

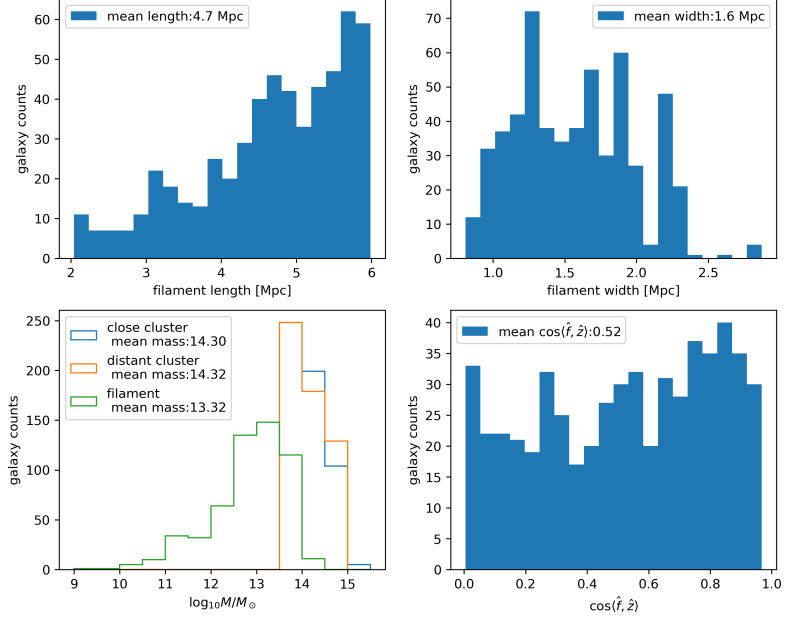


**Fig. A1** Filament properties (length, width, mass, alignment) of the results in Fig. 1 and 2, with the fiducial selections described in Sec. 5. By stacking the galaxies in each cluster-filament-cluster system, we find the mean length (cluster-cluster distance, top-left panel) is 4.7 Mpc, mean width (galaxy-filament axis distance, top-right panel) is 1.6 Mpc, mean filament mass is an order smaller than the cluster mass (bottom-left panel), and mean alignment angle between filament ( $\hat{f}$ , pointing from the low-z cluster to the high-z cluster) and line-of-sight direction ( $\hat{z}$ ) is  $\sim 60$  deg (bottom-right panel).

the deviation of the data vector from zero, i.e.  $\sqrt{\chi^2}$ . We tested the S/N calculation with the covariance ( $5.6\sigma$ ) or only the errorbar ( $5.8\sigma$ ). Since the number of subsamples (360) is significantly larger than the size of data vector (10), the calibration to the covariance is  $\sim 3\%$  and is negligible [45, 46].

As a further validation of the physics discovered in this work, as well as for identifying where the flow signal resides, we tested how the selection functions above (cluster richness  $\lambda_c$ , cluster mass  $M_c$ , filament richness  $\lambda_f$ , filament length  $L$  and filament width  $W$ ) affect the flow. The corresponding results are presented in Appendix B. We note the result in Fig. 2 is not the optimal but rather a conservative selection. By aggressively expanding the filament richness range, one can achieve  $S/N > 7\sigma$ .

## Appendix A Filament properties

Based on the fiducial selections of the cluster pairs and filaments described in Sec. 5, we present the mean filament properties in this section. As the filament flow is actually described by each  $\Delta z$  v.s.  $x$  pair, we treat each galaxy as equal weighted in every cluster-galaxy-cluster system, and the corresponding distribution in terms of filament length, width, cluster mass, filament mass, and filament alignment are presented in Fig. A1. Overall, we find the mean filament length is  $L = 4.7$  Mpc, width  $W = 1.6$

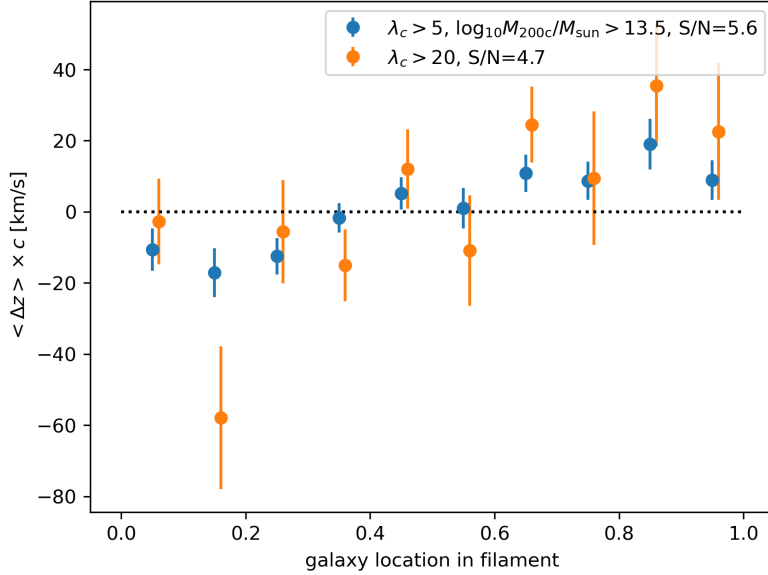


**Fig. B2** Comparison of different selections for the clusters. We see that pure richness selection (orange) can still yield a relatively strong S/N; however, the fitted slope (similar to that in Fig. 1) has only  $2\sigma$  significance, due to the limited number of galaxies. Thus it is not an ideal selection for understanding detailed flow behavior.

Mpc, cluster mass  $\log_{10}M_c/M_{\odot} \sim 14.3$ , filament mass  $\log_{10}M_f/M_{\odot} \sim 13.32$ , filament aligned  $\arccos(0.52) \sim 60$  deg with respect to the line-of-sight direction. We note the cluster mass and filament mass are calculated using the group mass of the designated galaxy. Since we require  $\lambda_c > 5$  for the cluster, its mass is relatively more reliable, while for the filament the selection of  $\lambda_f < 5$  could lead to extra bias[35]. In the future mass reconstructions with weak lensing for those systems could be very helpful.

## Appendix B Selection dependency

A conventional choice for a cluster is richness  $\lambda_c > 20$ ; however, in SDSS galaxy group data only a small fraction of groups can satisfy this cut. Additionally, richness is not strongly correlated with mass, owing to the substantial scatter [47]. We choose an alternative selection of  $\lambda_c > 5$  and  $m > 10^{13.5} M_{\odot}$ , where  $\lambda_c$  serves primarily to screen for reliable clusters [35], and use the optically obtained mass as the key selection. The comparison is shown in Fig. B2.

We check for the filament richness cut, in which a galaxy group not only must be located within a cylindrical space defined by the two clusters, but its richness must also satisfy  $1 < \lambda_f < 5$ . The choice of  $\lambda_f < 5$  is to distinguish filaments from clusters selection  $\lambda_c > 5$ , while the lower limit  $\lambda_f > 1$  is to minimize contamination from void regions where no filament exists between two clusters. Other choices of filament richness are shown in Fig. B3. We note that although the optimal case in terms of S/N

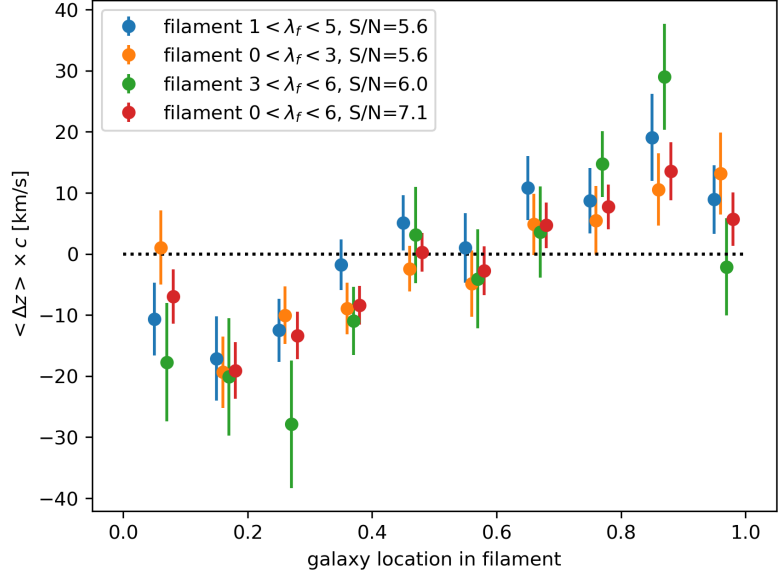


**Fig. B3** Comparisons of different filament richness cuts. The more obvious filaments ( $0 < \lambda_f < 3$ , orange) and less obvious filaments ( $3 < \lambda_f < 6$ , green) show significances similar to the default cut (blue), demonstrating that the filament flow widely exists. The aggressive cut ( $0 < \lambda_f < 6$ , red) can offer a more significant signal, however, we choose not to use it to ensure robustness.

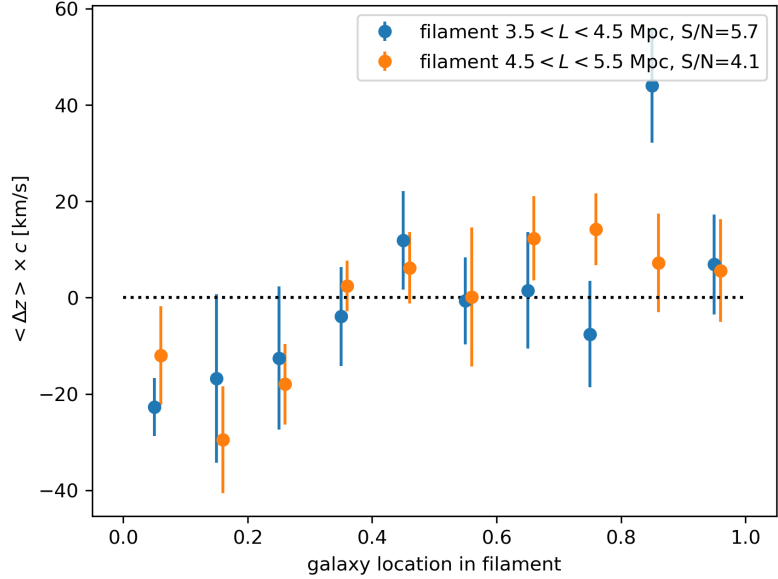


**Fig. B4** Comparisons of different filament length cuts. We find the majority of the filament flow signal comes from filament length  $L \sim 4$  and  $\sim 5$  Mpc. This is consistent with the general expectation for filament length. The longer or shorter filaments have significance  $\leq 3\sigma$ , and we exclude them for clarity. The filament flow in this figure is not symmetric due to the limited number of galaxies.

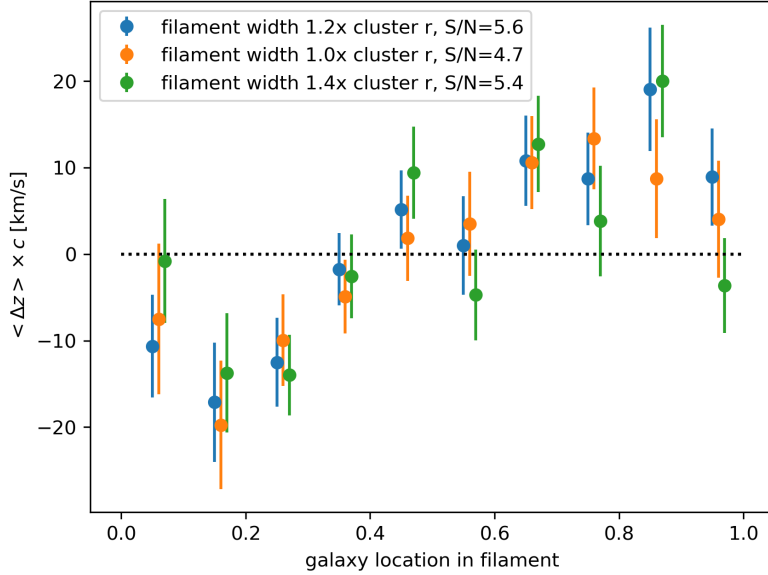


**Fig. B5** Comparisons of different choices for filament width. We see thinner filaments ( $1 \times r_{200c}$ , orange) or fatter filaments ( $1.4 \times r_{200c}$ , green) retain the main signal, but the fiducial choice ( $1.2 \times r_{200c}$ , blue) optimizes the significance, likely because it accommodates the possible meandering paths or nonlinear geometry of filaments.

$(\lambda_f < 6, \text{S/N} \sim 7)$  uses a larger filament sample, we adopt the default cut, to maintain consistency with our cluster definition.

Filament length is also an important property, as the flow velocity on a longer filament is lower due to weaker gravitational influence from the clusters, but a longer filament also means more member galaxies, which can reduce the noise. In Fig. B4, the highest S/N is found for filament length  $L \sim 4$  and  $\sim 5$  Mpc, which falls within a reasonable range, as a quick calculation of halo-matter correlation function<sup>4</sup> shows the 1-halo term is at  $< 1$  Mpc and the 2-halo term dominates around  $\sim 10$  Mpc, and we expect filaments to reside in between.

The last property we examine is the width of the filaments. We use  $1.2 \times r_{200c}$  as a fiducial choice, where  $r_{200c}$  is the radius of the cluster where the mean density is 200 times higher than the critical density of the Universe. Considering that filaments are not perfectly straight lines between clusters and our cylindrical selection is only a first-order approximation, we use  $1.2 \times r_{200c}$  to include possible zigzag shapes of filaments. Comparisons with alternative widths can be found in Fig. B5.

As a summary, we see our finding of filament flow is robust to multiple choices of the cluster-filament-cluster system, while some choices even provide stronger evidence than the fiducial choice. Due to the limitation of the current data, we defer other scientific questions and potential tests to future Stage-IV observations.

<sup>4</sup><https://github.com/czymbh/csstemu> [48], more specifically <https://github.com/czymbh/csstemu/blob/master/test/test-xihm.ipynb>

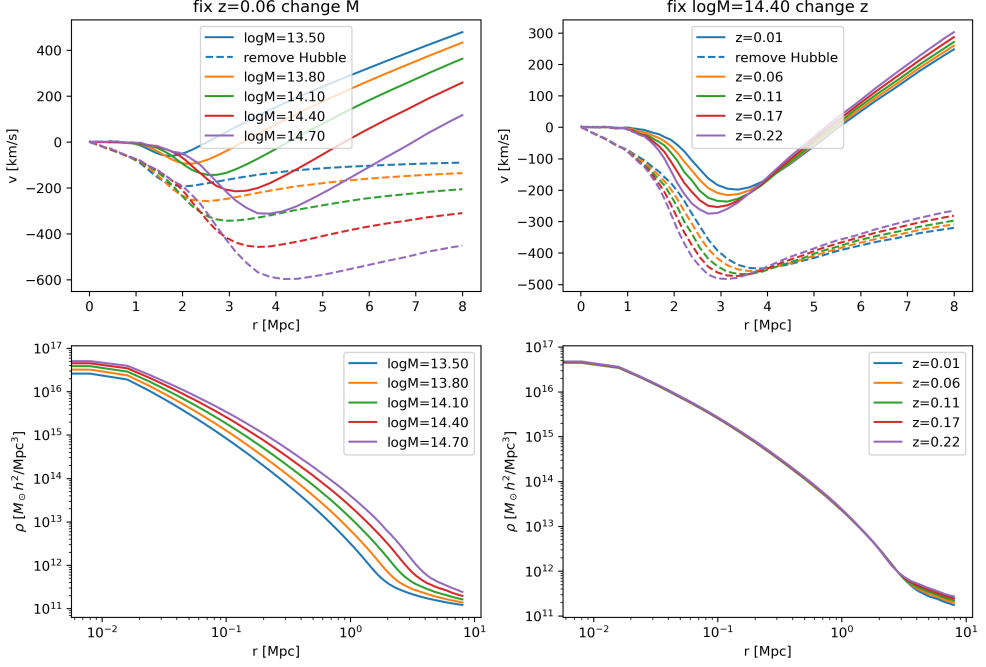


**Fig. C6** The emulator of the velocity profile and density profile of clusters/halos built from N-body simulations characterizing typical halo growth for the average cosmological environment. The top two panels show the velocity emulator  $v(z, M, r)$ , with top-left panel fixing redshift while letting the mass change, and top-right panel fixing the mass while letting the redshift change. Solid curves correspond to infall velocity plus Hubble flow, while dashed curves remove Hubble flow and leave only the infall velocity. The two bottom panels show the density emulator  $\rho(z, M, r)$ , with bottom-left fixing  $z$  and bottom-right fixing  $M$ . We note the above emulators use virial mass  $M_{\text{vir}}$  instead of  $M_{200c}$  in the data, and these mass definitions are bridged assuming a c-M relation [49].

## Appendix C Velocity emulator and model validation

We construct a velocity emulator from N-body simulation [4–6] to describe the general infall flow around clusters/halos, and use the emulator to construct a halo-halo-halo model to mimic the cluster-filament-cluster dynamics and compare with the filament flow in this work.

The simulation we use is one set from the CosmicGrowth Simulations [50], with a P<sup>3</sup>M code [51] run under WMAP  $\Lambda$ CDM cosmology ( $\Omega_b = 0.0445$ ,  $\Omega_c = 0.2235$ ,  $\Omega_\Lambda = 0.732$ ,  $h = 0.71$ ,  $n_s = 0.968$ , and  $\sigma_8 = 0.83$ ). The simulation box size is 600 Mpc/h with  $3072^3$  dark matter particles, and the softening length is 0.01 Mpc/h. The halos are processed with Friends-of-Friends (FoF) and then with HBT+ [34, 52] to get subhalos and their evolutionary histories. The halo catalog covers a virial mass range  $10^{11.5} < M_{\text{vir}}[M_\odot/h] < 3 \times 10^{15}$ , which the minimum mass corresponding to  $\sim 500$  dark matter particles.

To construct the emulator, we choose halos from 9 snapshots covering a redshift range  $0 < z < 3$ , and 9 mass bins covering  $10^{12} < M_{\text{vir}}[M_\odot/h] < 10^{15}$ . We linearly

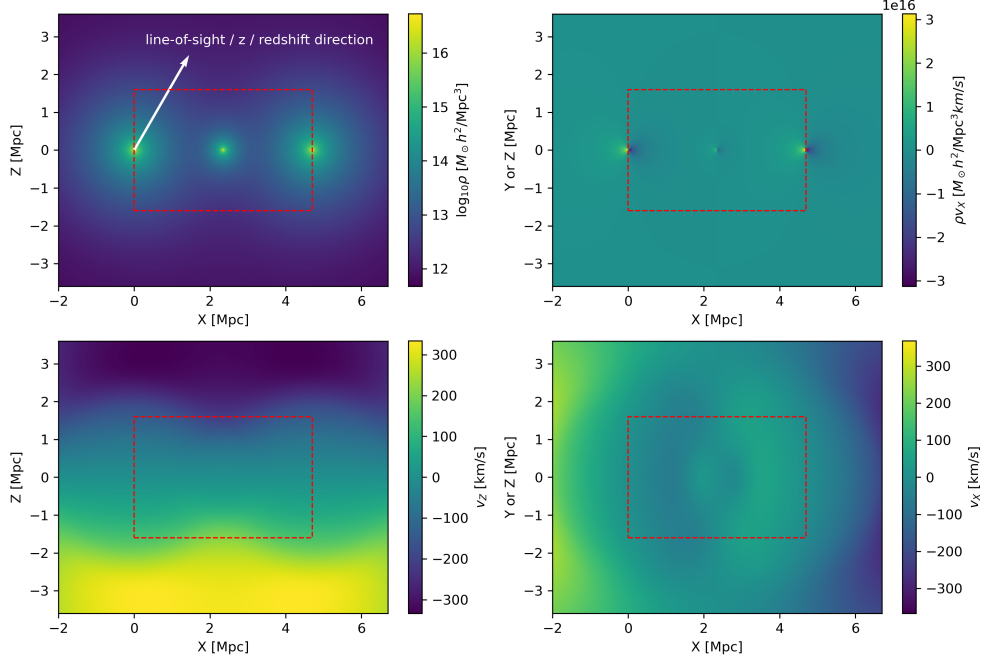


**Fig. C7** A halo-halo-halo model to mimic the desired cluster-filament-cluster dynamics. The top-left panel shows the spatial configuration of the three halos and their density  $\rho$  distribution, with two large halos ( $M_{200c} \sim 10^{14.3} M_\odot$ ) at two ends and a small halo ( $M_{200c} \sim 10^{13.32} M_\odot$ ) in the center. The z-direction (line-of-sight) is 60 deg to the X-axis (filament direction), while Y-axis and Z-axis are perpendicular to X-axis, and z-direction is on the X-Z plane. The top-right panel shows the  $\rho v_X$  distribution to describe the mass flow rate. The bottom-right panel shows the distribution of  $v_X$ , i.e. the velocity along the X-axis (along the filament), its integration over the Y-Z plane within the filament yields the velocity line-profile that we will show later in Fig. C8. The bottom-left panel shows the velocity along Z axis  $v_Z$ . All the panels show the 3D distribution at the central plane ( $Y = 0$  or  $Z = 0$ ) of the filament, while the red dashed box denotes the cylindrical selection function of the filament.

interpolate the velocity profile as a function of  $z$ ,  $\log_{10}(M_{\text{vir}}/M_\odot)$ , and comoving distance to the halo center  $r$  [Mpc]. The resulting velocity emulator  $v(z, M, r)$  is shown in the two top panels in Fig. C6. Similarly, the density emulator  $\rho(z, M, r)$  is constructed and shown in the two bottom panels in Fig. C6.

In addition, since the simulation uses  $M_{\text{vir}}$  while the observation uses  $M_{200c}$ , we use core cosmology library (CCL) [53] to convert different mass definition. During this process, a concentration-mass (c-M) relation needs to be assumed, and we compare two widely used models Duffy08 [54] and Diemer15 [49]. The different choices can lead to a  $\sim 3\%$  difference in mass conversion, which is negligible. We adopt the Diemer15 c-M relation to convert the observational  $M_{200c}$  to  $M_{\text{vir}}$  for use in the emulators.

Then we can build a halo-halo-halo model to mimic the cluster-filament-cluster system we are interested in. In Fig. C7 we stack three halos in a straight line, with two large halos of  $M_{200c} \sim 10^{14.3} M_\odot$  separated by 4.7 Mpc, and a small halo of  $M_{200c} \sim$

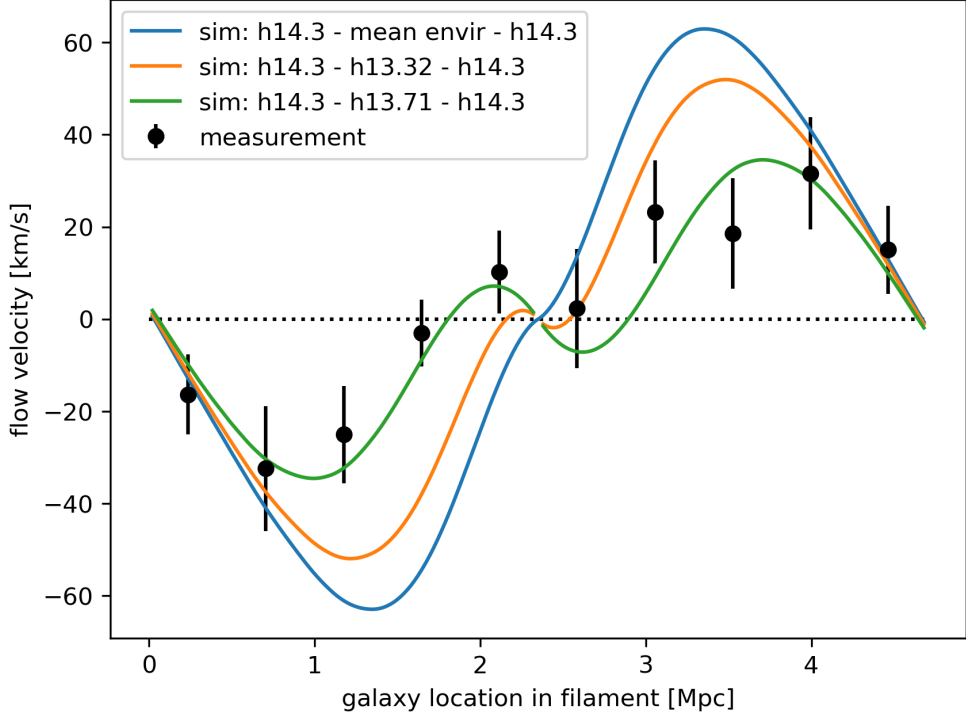


**Fig. C8** Deprojected velocity flow along the filament direction and comparisons with simulated data using the emulator from Fig. C6. The black data is the deprojected velocity  $v = v_z / \cos \langle \hat{f}, \hat{z} \rangle$ , derived from the measurements in Fig. 2 and A1. We see the peak infall velocity is  $\sim 30$  km/s. The three solid lines correspond to different filament setups, with two  $M_{200c} = 10^{14.3} M_\odot$  halos put at two ends, while put different halos in the center to represent the filament. The blue curve corresponds to the average cosmological environment, with no extra halo at the center. The orange curve includes an extra halo with  $M_{200c} = 10^{13.32} M_\odot$  (measured in Fig. A1) at the center, similar to Fig. C7. The green curve has an extra halo with  $M_{200c} = 10^{13.71} M_\odot$  at the center, shows perfect agreement with the observed velocity profile.

$10^{13.32} M_\odot$  at the center. We define the the X-axis as the filament direction, with the Y-axis and the Z-axis perpendicular to the X-axis. The line-of-sight direction, i.e. the z-direction, lies in the X-Z plane and is 60 deg to the positive X-axis. We estimate the overall 3D density distribution  $\rho_{\text{all}} = \sum_{i=1}^3 \rho_i(X, Y, Z)$  of the system, with  $i$  represents the i-th halo, and calculate the mass flow rate (MFR) in the X-direction, given by  $\text{MFR}_X = \sum_{i=1}^3 \rho_i v_{i,X}$ . Then a density-averaged velocity distribution is achieved by  $v_X = \text{MFR}_X / \rho_{\text{all}}$ . We show 3D distributions (on the 2D planes  $Y = 0$  or  $Z = 0$ , i.e., planes containing the central axis of the filament) of  $\rho_{\text{all}}$ ,  $\text{MFR}_X$ , and  $v_X$  in Fig. C7, where we also present  $v_Z$  calculated in a similar way.

To obtain the 1D flow projected on the X-axis, similarly to the 3D distributions above, we calculate by  $v_X^{\text{1D}} = \int_Z \int_Y \text{MFR}_X dY dZ / \int_Z \int_Y \rho_{\text{all}} dY dZ$ . Meanwhile, the observed flow  $v_z = c \Delta z$  in Fig. 2 is the flow projected on the z-direction, so the flow

deprojected on the filament is  $v = v_z / \cos\langle \hat{f}, \hat{z} \rangle$ . We note this calculation is also performed in each location bin, with jackknife resampling accounting for the variations in the cosine value, similar to the descriptions in Sec. 5. We compare the deprojected observational flow  $v$  and the simulated flow  $v_X^{1D}$  in Fig. C8. We see the simulation and observation agree in terms of flow profile shape and general peak velocity magnitude, which is an order of magnitude smaller than the single-halo situation in Fig. C6. However, when putting a  $M_{200c} \sim 10^{13.32} M_\odot$  halo in the center of the filament, the amplitude of the flow can differ by  $\sim 50\%$  from the observation. When we increase this mass to  $M_{200c} \sim 10^{13.71} M_\odot$ , the simulation and the observation perfectly fit, including the twisted shape in the middle, which is due to the self-gravitating infall flow of the smaller halo. This could be due to three different reasons: (1) the assumed WMAP cosmology is different from the real world; (2) the halo-halo-halo model we constructed is not a perfect reflection of the cluster-filament-cluster system, as halos are concentrated spherical objects, while filament should be more flat and elongated along X-axis; (3) the optically estimated  $M_{200c}$  in the group catalog might not be accurate when selecting richness  $\lambda_f < 5$  [35].

Nonetheless, we want to quantify the effect from RSD, given that the distance calculated in this work is in redshift space. The fact that the filament is aligned  $\sim 60$  deg to the z-direction makes the space distorted in a non-conventional way, unlike the typical Kaiser pancake or Finger-of-God shape. Moreover, the selection of cylindrical filament shape can affect the line-density. With the set-up in Fig. C7, we can calculate the RSD displacement field and see how the real-space constant density distribution transfers to redshift-space. This effect is visualized in Fig. C9, reflecting a twisted density distribution which is asymmetric around the X- or Z-axis. When selecting the cylindrical filament, its projected line-density on the X-axis is not a constant, shown in the bottom panel of Fig. C9. We see that the galaxy line-density in Fig. 1 deviates from constant density in real-space, confirming that its dip-peak-dip feature is due to the filament dynamics but not RSD. More importantly, the RSD induced non-uniform density corresponds to the flow in Fig. 2 and C8, but one visualized as RSD distance while the other visualized as velocity. This further confirms the observed velocity flow is gravity-originated.

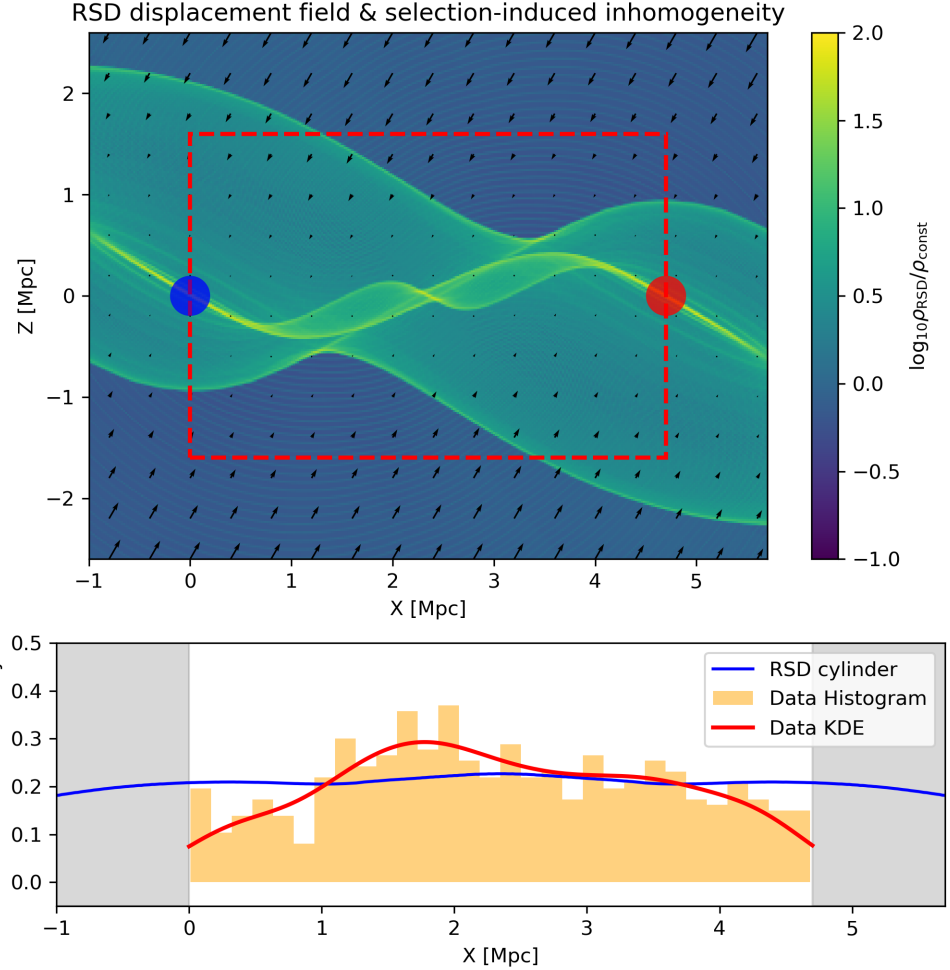


**Fig. C9** Impact from RSD and the cylindrical selection function. By construction the model from simulation (Fig. C7), we obtain the overall velocity field and project it on the line-of-sight  $z$ -direction. This projected peculiar velocity of this special system induces a redshift change, and will form redshift-space distortion (RSD). In the top panel, we show the RSD displacement field in black arrows (with amplitude normalized to a visual-friendly amount). Assuming the real-space is filled with constant density  $\rho_{\text{const}}$ , RSD will cause a inhomogeneous density distribution  $\rho_{\text{RSD}}$ , which we also show in the top panel. We calculate the line-density along the X-axis within the cylindrical selection function (red dashed box) and show it as the blue curve in the bottom panel. This demonstrates that the galaxy line-density in Fig. 1 is not due to the selection function, but due to the filament dynamics.